BAF facilitates interphase nuclear envelope repair through recruitment of nuclear transmembrane proteins.

Alexandra M. Young[1], Amanda L. Gunn[1], Emily M. Hatch[1*]

1. Division of Basic Sciences and Human Biology, The Fred Hutchinson Cancer Research Center, 1100 Fairview Ave, Seattle, Washington 98109, USA.

Running head: BAF promotes nuclear membrane repair

*Corresponding author
Emily Hatch
Phone: (206) 667-5116
E-mail: ehatch@fredhutch.org

Abstract

Nuclear membrane rupture during interphase occurs in a variety of cell contexts, both healthy and pathological. In the primary nucleus, membrane ruptures are rapidly repaired but the mechanisms are still unclear. Here we show that BAF, a nuclear envelope protein that shapes chromatin and recruits additional NE proteins in mitosis, also facilitates nuclear membrane repair in interphase, in part through recruitment of the nuclear membrane proteins emerin and LEMD2 to rupture sites. Using a cancer cell line depleted of lamin B1 to drive membrane rupture, we confirmed that GFP-BAF accumulates at rupture sites and found that BAF depletion increased the duration of nucleus integrity loss after rupture, with the largest effects being on longer ruptures. This phenotype could be rescued by WT BAF, but not by a mutant lacking the LEM-protein binding domain. Depletion of LEMD2 or emerin, but not lamin A/C, was sufficient to significantly increase the proportion of long ruptures, consistent with LEM-protein binding being a key function of BAF during membrane repair. Overall our results suggest a membrane repair model where BAF facilitates the repair of large membrane ruptures, in part by recruiting transmembrane nuclear envelope proteins, but where small ruptures are repaired by a BAF-independent mechanism.

Introduction

The nuclear envelope (NE) is a dynamic protein and membrane compartment that can lose and regain compartmentalization during interphase. Interphase nuclear membrane rupture generally occurs when mechanical stress causes chromatin or nucleoplasm to herniate through gaps in the nuclear lamina, the intermediate filament meshwork that provides mechanical support to the membrane. Tension on the membrane, which is no longer supported by the nuclear lamina meshwork, then leads to membrane rupture (Houthaeve *et al.*, 2018). In cells with an intact nuclear lamina, membrane rupture occurs in response to large stresses, such as migration through small pores in dense extra-cellular matrix or confinement between glass coverslips (Denais *et al.*, 2016; Raab *et al.*, 2016; Halfmann *et al.*, 2019). However, in cells where the nuclear lamina has been disrupted by lamina protein depletion or introduction of disease-associated mutations in the gene encoding lamins A and C, membrane rupture occurs in response to smaller forces, such as nuclear migration *in vivo* or growth on tissue culture plastic (De Vos *et al.*, 2011; Vargas *et al.*, 2012; Tamiello *et al.*, 2013; Hatch and Hetzer, 2016; Penfield *et al.*, 2018; Earle *et al.*, 2019).

Several model systems have been developed to investigate the consequence of nuclear membrane rupture. Membrane ruptures from confined migration or mechanical disruption, such as laser wounding, tend to be large and last longer than ruptures induced by lamina disruption and growth on stiff surfaces (De Vos *et al.*, 2011; Vargas *et al.*, 2012; Tamiello *et al.*, 2013; Denais *et al.*, 2016; Raab *et al.*, 2016; Penfield *et al.*, 2018; Halfmann *et al.*, 2019). In both cases, nuclear membrane ruptures are repaired and generally non-lethal (De Vos *et al.*, 2011; Vargas *et al.*, 2012; Denais *et al.*, 2016; Raab *et al.*, 2016). However, recent studies suggest that loss of nuclear compartmentalization can alter transcription (De Vos *et al.*, 2011), cause mislocalization of large organelles (De Vos *et al.*, 2011; Vargas *et al.*, 2012; Houben *et al.*, 2013), and cause DNA damage (Maciejowski *et al.*, 2015; Denais *et al.*, 2016; Raab *et al.*, 2016; Irianto *et al.*, 2017; Takaki *et al.*, 2017; Pfeifer *et al.*, 2018; Stephens *et al.*, 2019). Based on these data, nuclear membrane rupture is now being evaluated as a major mechanism of genome instability and cell death in lamin-associated diseases and cancer (Isermann and Lammerding, 2017; Houthaeve *et al.*, 2018).

Efficient repair of the nuclear membrane is likely critical for cell viability after rupture and current research suggests that this mechanism uses many of the same proteins as NE assembly at the end of mitosis. Several proteins that accumulate on the chromatin during NE assembly (reviewed in (LaJoie and Ullman,

2017)) also accumulate on exposed chromatin at membrane rupture sites, including BAF (barrier to autointegration factor), lamin A, LEM-domain nuclear transmembrane proteins (NETs), and the ESCRT-III membrane remodeling complex (Denais *et al.*, 2016; Raab *et al.*, 2016; Penfield *et al.*, 2018; Halfmann *et al.*, 2019). During NE assembly, BAF cross-links the chromatin mass to promote formation of a single nucleus (Samwer *et al.*, 2017) and recruits lamin A and LEM domain NETs (Haraguchi *et al.*, 2001; Margalit *et al.*, 2005; Haraguchi *et al.*, 2008; Appen *et al.*, 2019), which bring ER membrane to the decondensing chromatin. BAF has been shown to be required for membrane repair during ruptures induced by cell migration through small pores and laser wounding, and this function is specific to its ability to recruit new membranes through accumulation of NET proteins (Halfmann *et al.*, 2019). During NE assembly, BAF also promotes membrane resealing through recruitment of LEMD2, which binds the ESCRT-III protein Chmp7 (Webster *et al.*, 2014; Olmos *et al.*, 2016; Gu *et al.*, 2017; Appen *et al.*, 2019). Loss of ESCRT-III delays membrane repair in some systems, but not others (Denais *et al.*, 2016; Raab *et al.*, 2016; Halfmann *et al.*, 2019; Penfield *et al.*, 2019). Thus, a current model of membrane repair is that, like NE assembly, nucleus recompartmentalization requires recruitment of ER membranes, via interactions between LEM-domain proteins with chromatin-bound BAF, and that ESCRT-III facilitates resealing in specific conditions.

However, this model of nuclear membrane repair has been developed through analysis of large rupture events, either after forced cell migration through very small pores or laser wounding of the nucleus surface (Denais *et al.*, 2016; Raab *et al.*, 2016; Halfmann *et al.*, 2019). It remains unclear whether this NE assembly-like mechanism is required to repair all membrane ruptures, specifically smaller ruptures that occur under less force and may be more relevant to laminopathy phenotypes (De Vos *et al.*, 2011; Earle *et al.*, 2019; Zhang *et al.*, 2019). In addition, these data strongly suggest the existence of two pathways of membrane repair, one that requires ESCRT-III activity and one that does not, and it is unclear how distinct these two pathways are and under what conditions each one is normally used.

To address these questions and define the mechanism of membrane repair in a broader context, we turned to a nuclear membrane rupture system based on depletion of lamin B1 in U2OS cells. Our previous work in these cells suggested that lamin B1 depletion reduces the amount of force required for rupture by increasing the size and frequency of gaps in the nuclear lamina and results in multiple spontaneous ruptures covering a range of sizes in individual nuclei (Hatch and Hetzer, 2016). Unlike lamin A (Denais *et al.*, 2016;

Raab *et al.*, 2016; Halfmann *et al.*, 2019), the B-type lamins do not accumulate at membrane rupture sites (Denais *et al.*, 2016), making this cell line ideal for membrane repair studies.

In a preliminary analysis of nuclear lamina protein recruitment to membrane rupture sites, BAF showed a striking and reliable accumulation at rupture sites. To follow up on this observation, we characterized BAF recruitment and kinetics at rupture sites and its function in membrane repair. Our data indicate that BAF marks ruptures of all sizes and that its release from chromatin is partially dependent on membrane repair. We also found that BAF is not required for membrane repair after rupture but does reduce the number and duration of very long ruptures. This function requires the LEM-domain binding motif in BAF, consistent with previous results (Halfmann *et al.*, 2019), and depletion of the NETs emerin or LEMD2 partially phenocopies BAF depletion. Unexpectedly, we found that BAF depletion did not affect all ruptures equally. Very short, small ruptures repaired with similar efficiency in the presence or absence of BAF, and, even more surprisingly, repaired slightly faster when LEM protein recruitment was inhibited. Thus, our data strongly suggest that there are two membrane repair pathways, one of which is BAF-dependent and one of which is impaired by BAF-dependent LEM protein recruitment, that are used to repair small versus large membrane ruptures.

Results and Discussion

To characterize BAF kinetics from a range of membrane rupture sizes, we stably expressed GFP-BAF, 2xRFP-NLS (NLS = nuclear localization signal) and shRNAs against lamin B1 (shLmnB1) in U2OS cells. Depletion of lamin B1 was confirmed by western blot and immunofluorescence and caused an increase the number and size of nuclear lamina gaps, as expected (Figure S1, A and B). 2xRFP-NLS (RFP-NLS) localizes to the nucleus when the membrane is intact. When the membrane ruptures, RFP-NLS becomes visible in the cytoplasm and its intensity in the nucleus decreases. The site where cytoplasmic RFP-NLS first appears marks the site of nuclear membrane rupture and the degree of RFP-NLS loss defines the extent of the rupture, which is indicative of the size of the membrane gap (Denais *et al.*, 2016; Raab *et al.*, 2016; Deviri *et al.*, 2019; Zhang *et al.*, 2019). During rupture, RFP-NLS is continually diffusing out of the membrane gap and being reimported by nuclear pores around the rest of the membrane. As nucleus integrity is restored, the rate of diffusion decreases and RFP-NLS intensity in the nucleus (RFP-NLS_{Nuc}) begins to increase. When the membrane is completely sealed, any remaining RFP-NLS in the cytoplasm is reimported and the nuclear intensity returns to

pre-rupture levels. RFP-NLS intensity during recovery is best fit to a sigmoid curve, the same as what is observed during NE assembly as nuclear import starts prior to membrane resealing (Anderson and Hetzer, 2008; Vargas *et al.*, 2012).

To determine GFP-BAF kinetics during rupture and repair, we first arrested U2OS RFP-NLS shLmnB1 GFP-BAF cells for 24 hr to block mitosis and increase the frequency of membrane rupture (Hatch and Hetzer, 2016), then imaged cells either every 30 sec for 4 hr or every 3 min for 24 hr by live-cell imaging. Using RFP-NLS to mark the time and site of membrane rupture, we found that GFP-BAF was rapidly (within 30 sec) recruited to membrane rupture sites, followed by a gradual decrease in GFP-BAF intensity until a plateau was reached (Figure 1, A-C; Movie S1-2). This plateau was frequently higher than the GFP-BAF intensity in the surrounding NE (50/58 ruptures; Figure1, D and E, Movie S3), marking the site of membrane rupture for as long as 22 hrs after RFP-NLS nuclear reaccumulation. We observed distinct GFP-BAF foci for every rupture, even when multiple ruptures clustered either spatially or temporally (Figure S1, C and D, Movie S5-6). Although a clear decrease in RFP-NLS_{Nuc} was not always visible in the intensity traces (e.g. Figure S1D, Movie S3), each accumulation of GFP-BAF was accompanied by the appearance of RFP-NLS in the cytoplasm (Figure S1D, Movie S3). In addition, within an individual cell, the amount of GFP-BAF recruited during the rupture correlated with the extent of RFP-NLS mislocalization to the cytoplasm (Figure 1B). Previous studies demonstrated that BAF is temporarily recruited to rupture sites (Denais *et al.*, 2016; Liu *et al.*, 2018; Halfmann *et al.*, 2019). Our data are consistent with this observation, and in addition we find that GFP-BAF is a sensitive and accurate marker of both the occurrence and size of interphase nuclear membrane rupture events that can mark the site of cytoplasmic-exposed chromatin for many hours after membrane repair.

We next asked whether GFP-BAF removal required re-establishment of membrane integrity. First we determined the timing of GFP-BAF loss from rupture sites by averaging RFP-NLS_{Nuc} and GFP-BAF intensity measurements of ruptures of similar durations (time from the first decrease in RFP-NLS_{Nuc} intensity), and comparing when GFP-BAF began to decrease after rupture to when RFP-NLS_{Nuc} began to increase. We found that the majority of membrane rupture sites lost GFP-BAF fluorescence prior to the start of RFP-NLS reaccumulation (Figure 1C, arrows). This difference was even more evident for longer ruptures (Figure S1E, arrows). This suggested that GFP-BAF removal did not require the initiation of membrane repair. We next examined GFP-BAF recruitment to ruptured micronuclei to determine whether membrane repair has an effect

on the extent or rate of GFP-BAF loss. Micronuclei (MN) form in human cells when chromosomes missegregate during mitosis and recruit their own nuclear envelope. In contrast to the primary nucleus, nuclear membrane ruptures in MN are rarely able to repair (Hatch *et al.*, 2013). Analysis of live-cell imaging of micronucleated cells, generated by addition of the spindle checkpoint inhibitor, reversine (Santaguida *et al.*, 2010), showed that GFP-BAF accumulated on ruptured MN concurrently with the disappearance of RFP-NLS, and remained accumulated on the exposed chromatin until the end of imaging or mitosis (Figure S1F, Movie S1, S4) (Liu *et al.*, 2018). In addition, GFP-BAF frequently accumulated at a single focus on the MN and then spread throughout the chromatin (Figure 1G, 53/56 MN). Analysis of the average rate and extent of GFP-BAF intensity loss on MN showed that GFP-BAF loss from MN was significantly slower than loss from primary nucleus rupture sites and plateaued at a higher intensity (Figure 1G, Movie S1). Together these data suggest that BAF removal from rupture sites begins prior to nuclear recompartmentalization but is responsive to membrane repair.

Based on BAF's recruitment to membrane rupture sites and its multiple functions in restoring nuclear membrane integrity during mitotic exit (Jamin and Wiebe, 2015), we examined the function of BAF in nuclear membrane rupture and repair. U2OS shLmnB1 RFP-NLS cells were transfected with siRNAs against BAF (siBAF) or a control siRNA (siControl) for 24 hr, then arrested for an additional 24 hr with hydroxyurea, before live-cell images were taken every 3 min for 24 hr. BAF protein levels were significantly reduced 48 hr after siRNA transfection (Figure 2A) and this early time point avoided mitotic phenotypes associated with BAF depletion, including extensive mislocalization of lamin A/C and emerin from the NE and lobulated nuclei or multinucleation (Haraguchi *et al.*, 2008; Samwer *et al.*, 2017) (Figure S2, A and B). We first analyzed the frequency of nuclear membrane rupture in cells depleted of BAF versus control. We found that there was no difference in the proportion of nuclei that underwent at least 1 rupture event or in the number of ruptures per cell (Figure S2, C and D), indicating that BAF does not contribute to rupture frequency.

We next analyzed how many nuclei were able to fully recompartmentalize after rupture, defined as the absence of RFP-NLS in the cytoplasm. Unexpectedly, we found that 97% (99/102) of siControl cells and 98% (84/86) of siBAF cells fully recovered RFP-NLS$_{Nuc}$ after each rupture. In contrast to what was previously observed (Halfmann *et al.*, 2019), these data strongly suggest that BAF is not required for membrane repair or cell viability during long membrane ruptures. We then quantified the duration of nuclear integrity loss during

rupture events (defined by cytoplasmic RFP-NLS, see methods, Figure 2B) in BAF-depleted cells. We found that BAF depletion significantly increased the duration of nuclear integrity loss compared to control cells (Figure 2C, Movie S1 and S7-8). This phenotype was specific to BAF, as expression of GFP-BAF in cells transfected with siBAF restored the median duration of nuclear integrity loss to control levels (Figure S2, G and H), and did not depend on knockdown of LmnB1 (Figure S2, E and F). These data strongly suggest that at least two membrane repair pathways exist, one of which functions independently of BAF. This result also implies that there are different types of ruptures whose physical properties or cellular context require different repair mechanisms to efficiently restore compartmentalization.

To determine whether all ruptures are equally affected by BAF depletion, we compared the proportion of ruptures at each duration of nuclear integrity loss between BAF depleted cells and control cells. To facilitate analysis, we binned “very long” ruptures, defined as nuclear integrity loss greater than or equal to 30 min (top 5% of control ruptures) together. As expected, we found that the proportion of very long ruptures was highly elevated in siBAF cells. However, very short ruptures (nuclear integrity loss = 3 min or less) were only modestly affected (Figure 2D). These very short ruptures frequently occurred in the same nuclei as very long ruptures (Figure S2I), indicating that this result cannot be explained by transfection efficiency. In addition, this result is unlikely to be due to sub-3 min ruptures becoming newly visible in our live-cell imaging assay after BAF depletion. Analysis of nuclear integrity loss using a 30 sec pass time instead of 3 min showed that only 7% of ruptures reaccumulated RFP-NLS in under 3 min (5/69) and that the median duration of integrity loss for these ruptures was 2 min. Therefore, a 3 min pass time would miss, on average, only 1% of ruptures, which would still result in a significant persistence of very short ruptures after BAF depletion. Thus, we infer that very short membrane ruptures are repaired with similar efficiency in the presence and absence of BAF whereas, without BAF, membrane repair is significantly delayed in ruptures lasting longer than a few minutes. Together these data strongly suggest that different mechanisms are required to repair ruptures of different sizes.

To determine whether the delay in RFP-NLS recovery after BAF depletion is due to defects in initiating membrane repair, defects in membrane sealing, or a defect in nuclear import during repair we analyzed the timing and kinetics of RFP-NLS_{Nuc} recovery during very long ruptures in siBAF and siControl transfected cells. We reasoned that if initiation of membrane repair was defective in very long ruptures, the duration of rupture (time that RFP-NLS_{Nuc} = intensity minimum) would lengthen, whereas if membrane resealing or nuclear import

were defective, the duration of recovery (time between RFP-NLS$_{Nuc}$ minimum and the recovery plateau (Figure 2E)) would lengthen. Almost all RFP-NLS$_{Nuc}$ intensity traces during recovery of very long ruptures were best fit by a sigmoidal curve (8/9), indicating that we can visualize the initial stages of recompartmentalization in our assay. First, we assessed whether BAF depletion affected the efficiency of membrane resealing or nuclear import by comparing RFP-NLS$_{Nuc}$ recovery durations in siBAF versus siControl cells. We found that BAF depletion did not affect the duration of RFP-NLS$_{Nuc}$ recovery during very long ruptures (Figure 2, E and F). As expected, the duration of RFP-NLS recovery correlates with the duration of nucleus integrity loss for shorter ruptures, which show a strong correlation between rupture duration and extent of RFP-NLS$_{Nuc}$ loss (compare Figure 1C to Figure S1E), and (Robijns *et al.*, 2016)), and plateaus for ruptures that lose nucleus integrity for over 30 min, which show a maximum 70% loss of initial RFP-NLS$_{Nuc}$ intensity (Figure 2E). Next we asked whether increased duration of rupture was sufficient to explain longer losses of nucleus integrity in both control and BAF depleted cells by comparing the duration of rupture in the combined population to the duration of nuclear integrity loss. In contrast to recovery duration, we found that rupture duration strongly correlated with nuclear integrity loss duration (Figure 2, E and F) at all time points. These data indicate that loss of BAF delays the initiation of recompartmentalization during ruptures lasting longer than a few minutes and validate that using the length of nuclear integrity loss is a robust proxy for rupture duration in these cells.

We also frequently observed RFP-NLS$_{Nuc}$ recovering to higher mean intensity than pre-rupture values accompanied by a decrease in nucleus volume (Figure S2J), consistent with chromatin compaction during very long ruptures (Robijns *et al.*, 2016). This phenotype was observed in both siControl and siBAF cells (Figure 2E), suggesting that BAF DNA-cross-linking is not driving compaction of chromatin during membrane rupture (Hatch *et al.*, 2013; Robijns *et al.*, 2016).

To determine whether the ability of BAF to bind LEM-domain NETs facilitates membrane repair of longer ruptures, we asked whether a mutation that blocks the LEM-domain binding site in BAF (L58R (Samwer *et al.*, 2017)) can rescue BAF depletion. L58R-GFP-BAF- was stably expressed in U2OS RFP-NLS shLmnB1 cells (Figure 3A), and as expected (Samwer *et al.*, 2017), showed decreased recruitment to the NE in interphase (Figure 3B) yet accumulated as frequently as WT-GFP-BAF at membrane rupture sites, even in the absence of endogenous BAF (Figure 3C, Movie S9-10). The duration of nucleus integrity loss was analyzed in this cell line by live-cell imaging after siBAF transfection and compared to cell lines stably expressing either

GFP alone or WT-GFP-BAF that were similarly depleted. We found that GFP-BAF-L58R expression decreased the median duration of nuclear integrity loss compared to GFP alone (Figure 3D), but did not reproducibly decrease the proportion of very long ruptures (Figure 3E), suggesting that loss of the LEM-binding region of BAF significantly impairs its ability to restore nucleus integrity in longer ruptures.

BAF interacts with several proteins that accumulate at rupture sites, including lamin A/C, emerin, and LEMD2 (Denais *et al.*, 2016; Halfmann *et al.*, 2019). To determine which BAF binding partner(s) contributes to efficient membrane repair, we first asked which proteins required BAF to accumulate at sites of membrane rupture. Using immunofluorescence and either the presence of cytoplasmic RFP-NLS or a nuclear cGAS focus (Denais *et al.*, 2016; Raab *et al.*, 2016) to identify ruptured nuclei, we assessed whether emerin, lamin A/C, or LEMD2 localized to membrane rupture sites after BAF depletion. Confirming previous results (Halfmann *et al.*, 2019), we found that these proteins consistently localized to rupture sites in control cells but were absent when BAF was depleted (Figure 4A). To determine whether protein recruitment could be delayed rather than lost, we then imaged U2OS cells stably expressing shLmnB1, 3xGFP-NLS, and mCherry-LmnA by live-cell imaging and analyzed the proportion of ruptures that recruited mCherry-LmnA in cells transfected with siControl or siBAF. mCherry-LmnA accumulated at the site of each rupture, regardless of rupture size, in 100% of cells treated with siControl (27/27), but in only 6% of cells treated with siBAF (2/34, Figure S3A, Movie S11-12). Together these data indicate that BAF is required to recruit both LEM-domain NETs and lamin A to the sites of membrane ruptures.

To determine whether depletion of emerin, lamin A/C, or LEMD2 phenocopied the extended duration of nucleus integrity loss observed after BAF depletion. U2OS RFP-NLS shLmnB1 cells were transfected with siRNAs against each protein individually and the duration of nucleus integrity loss was analyzed by live-cell imaging 48 hr after siRNA transfection and 24 hr after hydroxyurea arrest. siRNA transfection was sufficient to deplete the targeted proteins to at least 30% of control levels by western blot (Figure S3B) and the majority of cells showed little to no protein expression by immunofluorescence (Figure S3, C-E). Depletion of each protein caused a statistically significant increase in the median duration of nucleus integrity loss, but only depletion of emerin or LEMD2 partially phenocopied the increased proportion of very long ruptures observed after BAF depletion (Figure 4C, Movie S13-15). Lamin A/C depletion caused a modest, but statistically significant, increase in the proportion of very long ruptures (Figure S3F) that likely reflects an overall increase in rupture

size (Denais *et al.*, 2016; Zhang *et al.*, 2019). Similar to BAF depletion, loss of emerin and LEMD2 did not cause a decrease in the proportion of very short ruptures; in fact LEMD2 depletion caused a consistent increase in this population (Figure 4C).Thus, our results suggest that recruitment of emerin and LEMD2 by BAF to sites of membrane rupture is required for efficient repair of longer ruptures.

Our results confirm that focal BAF accumulation on the nuclear envelope is an accurate and sensitive marker of nuclear membrane rupture (Denais *et al.*, 2016; Liu *et al.*, 2018; Halfmann *et al.*, 2019). We find that the amount of GFP-BAF recruited to the exposed chromatin correlates with the severity of the rupture, as seen previously (Denais *et al.*, 2016), and likely the size of the membrane hole (Zhang *et al.*, 2019), and that GFP-BAF remodeling occurs prior to membrane repair, but is accelerated by it. Our data are consistent with work in other systems that suggest that non-phosphorylated BAF is recruited to exposed chromatin from the cytoplasm and then released following inhibitory phosphorylation by nuclear kinases (Halfmann *et al.*, 2019). In our model, membrane recruitment could accelerate GFP-BAF removal by either passively increasing kinase concentration by nucleus resealing or actively targeting regulatory proteins to BAF-associated chromatin, similar to the correlation between membrane spreading and BAF release from chromatin during mitotic exit (Samwer *et al.*, 2017). An alternative or additional hypothesis is that BAF remodeling at rupture sites reflects the membrane remodeling activity of the ESCRT-III complex, which drives LEMD2 spreading over the chromatin after micronucleus rupture (Vietri *et al.*, 2019), similar to what we observe for BAF (Figure 1F). We observed that large BAF foci are frequently unable to disassemble completely after nuclear integrity is restored, and consistent with previous observations of lamin A (Denais *et al.*, 2016), we find these rupture-induced BAF “scars” are refractory to re-rupture. Since these scars are frequently adjacent to sites of re-rupture, it remains to be seen whether these stabilized membrane areas increase the overall stability of the membrane by reforming the nuclear lamina at rupture sites or cause local destabilization of the membrane.

Our data suggest a model of membrane repair where BAF is central to one of at least two mechanisms that can re-compartmentalize the nucleus after membrane rupture and where BAF functions specifically at large ruptures to increase the recruitment of transmembrane nuclear envelope proteins (NETs) to the site of exposed chromatin. In contrast to previous results (Halfmann *et al.*, 2019), we find that BAF is not required for nuclear membrane repair and that depletion of the LEM-domain proteins emerin or LEMD2, both of which require BAF to localize to rupture sites (Figure 4A, (Halfmann *et al.*, 2019)), is sufficient to significantly delay

repair of larger ruptures (Figure 4, B and C, Movie S14). Our observation that BAF depletion does not eliminate very short ruptures (3 min or less) suggests that different types of ruptures have different requirements for recompartmentalization. One potentially significant difference between very short ruptures and longer ones is the size of the membrane gap. Smaller ruptures are associated with smaller membrane holes (Denais *et al.*, 2016; Zhang *et al.*, 2019), and repair faster in our assays (Figure 1). The physical size of these holes could necessitate different mechanisms of membrane repair or correlate with different mechanisms of membrane instability, such as local detachment from an intact lamina versus expansion at the site of chromatin herniation through a lamina gap (Deviri *et al.*, 2019). Alternatively, the BAF-independent repair mechanism could be the same as the BAF dependent one, just slower due to a reliance on the ability of NETs to bind DNA and chromatin directly (Barton *et al.*, 2015). Together, our findings provide a new model that can be used as an entry point to identify additional mechanisms of interphase nuclear membrane repair.

An unexpected result from our data was the increase in the proportion of very short ruptures in LEMD2 depletion experiments. One possibility is that over-recruitment of LEMD2, or other NETs, could inhibit nuclear recompartmentalization through overactivation of ESCRT-III or excessive membrane recruitment. These conditions are both correlated with either the loss of nuclear membrane integrity or the prevention of membrane sealing after cell division or rupture (Appen *et al.*, 2019; Penfield *et al.*, 2019; Thaller *et al.*, 2019; Vietri *et al.*, 2019). Thus, the release of BAF from exposed chromatin during nuclear membrane rupture may be as critical as its recruitment to maintaining nucleus integrity.

NET accumulation in response to BAF localization could promote repair of large membrane gaps in two ways. First, BAF-dependent accumulation of LEMD2 could recruit ESCRT-III and remodel the membrane, and second, BAF could increase membrane recruitment to rupture sites (Halfmann *et al.*, 2019), which could plug the gap prior to membrane remodeling (Penfield *et al.*, 2019). Both mechanisms may contribute to membrane repair in our system, but our results favor a model where the main function of BAF is to recruit or stabilize additional membrane at large rupture sites. First, although LEMD2 depletion has a strong repair defect, consistent with ESCRT-III activity increasing repair efficiency (Denais *et al.*, 2016; Raab *et al.*, 2016), we also find that loss of emerin significantly increases the proportion of very long ruptures, suggesting that the membrane recruitment function of LEMD2 is more critical (Figure 4C). In support of this, LEMD2 and its binding partner, Chmp7, were recently suggested to have ESCRT-III independent functions in nuclear

compartmentalization following mitosis and membrane rupture (Appen *et al.*, 2019; Penfield *et al.*, 2019). Second, our data suggest that efficient sealing of small membrane gaps does not require BAF or LEMD2 (Figures 2D and 4C). This conflicts with an ESCRT-III dependent membrane repair mechanism since ESCRT-III is generally thought to be effective for fusing only small membrane holes (Gatta and Carlton, 2019). Finally, kinetic analysis of RFP-NLS$_{Nuc}$ recovery in BAF depleted cells (Figure 2, E and F) suggests that increased rupture duration is due to defects in the initial stage of membrane repair rather than the final sealing of small gaps, defects in which result in a slow leak of nuclear proteins (Olmos *et al.*, 2015; Vietri *et al.*, 2015). Together our data are most consistent with BAF being critical to recruit new membranes to the site of large ruptures to rapidly restore compartmentalization.

MATERIALS AND METHODS

Cell culture

U2OS cells were cultured in Dulbecco's modified Eagle medium (DMEM; GIBCO) supplemented with 10% (v/v) fetal bovine serum (FBS; GIBCO), and 1% (v/v) penicillin-streptomycin (Sigma-Aldrich) at 37°C with 10% CO_2 in a humidified incubator.

Construction of stable cell lines

U2OS RFP-NLS cells were made by transfecting U2OS cells with 2xRFP-NLS, selecting with 0.5 mg/ml G418 and collecting the RFP+ population by FACS. U2OS RFP-NLS EGFP-BAF shLmnB1 cells were made by infecting U2OS RFP-NLS cells with lentiviruses containing pLKO.1 shRNA-LmnB1.71 or EGFP-BAF-IRES-Blast vectors, selecting with10 µg/ml blasticidin (InvivoGen) and 2 µg/ml puromycin (Sigma-Aldrich) and sorting for RFP/GFP double positive cells by FACS.

Plasmids

All plasmids encoding EGFP-BAF (EGFP-BAF_WT, EGFP-BAF_L58R, EGFP-BAF_G47E and EGFP-BAF_G25E) were a gift from the Gerlich lab (IMBA, Vienna, Austria) and described in (Samwer *et al.*, 2017). The EGFP-BAF-IRES-Blast cassettes are expressed under the control of a crippled EF1α promoter. EGFP-IRES-Blast was generated by digesting EGFP-BAF_WT with XbaI and BamHI to remove EGFP-BAF inserting and EGFP-only was PCR'd and inserted via sequence- and ligation-independent cloning (SLiC). Lamin B shRNAs were expressed from the lentiviral plasmid pLKO.1 shRNA-LmnB1.71 puro (SHCLND-NM_005573, Sigma-Aldrich). The sequence of the lamin B1 shRNA is 5′ CCGGGCATGAGAATTGAGAGCCTTTCTCGAGAAAGGCTCTCAATTCTCATGCTTTTT-3′. 2xRFP-NLS (RFP-NLS) was described previously (Hatch *et al.*, 2013) and made by recombination of a PCR of TagRFP (Evrogen) fused to a C-terminal NLS (PPKKKRKV) into the Gateway vector pDONOR20 and recombining into pcDNA-DEST53-mCherry to generate mCherry-TagRFP-NLS.

siRNA transfection

All siRNA transfections were performed using siLentFect (Bio-Rad) according to manufacturer's instructions. Custom siRNAs (Dharmacon) against human BAF (#1. 5′-AGUUUCUGGUGCUAAAGAAtt-3′, #2. 5′-CCCUCACUUUCAAUCCGUUuu-3′), lamin A/C (5′-GGUGGUGACGAUCUGGGCUuu-3′)(Harada *et al.*, 2014), emerin (5′-GGUGCAUGAUGACGAUCUUtt-3′) (Salpingidou *et al.*, 2007), and LEMD2 (#1. 5′-UUGCGGUAGACAUCCCGGG[dT][dT] -3′, #2. 5′-UACAUAUGGAUAGCGCUCC[dT][dT] -3′) and a nontargeting control against Luciferase (5′-UAUGCAGUUGCUCUCCAGC[dT][dT] -3′) were used for gene knockdowns. siRNAs were added to 100 nM final concentration. Cells were analyzed 48 hr after a single siRNA transfection at t = 0 hr for all proteins except LEMD2, where cells were transfected at 0 and 24 hr.

Immunoblotting
Cells were lysed directly in 1x SDS/PAGE sample buffer (LC2570; Thermo Fisher Scientific) + βME and lysates were separated on 4–15% gradient gels (Mini-PROTEAN TGX; Bio-Rad) and transferred to nitrocellulose membrane (0.2 µm; Bio-Rad). Membranes were blocked with 5% (w/v) milk and 0.25% (v/v) Tween 20 in TBS for 1 hr, then incubated with appropriate primary antibodies. Primary antibodies were detected using HRP-conjugated secondary antibodies and enhanced chemiluminescence (SuperSignal West Femto Chemiluminescent Substrate; Thermo Fisher Scientific), or near-infrared–fluorescent conjugated secondary antibodies and a Li-Cor Odyssey fluorescence scanner. For blots imaged on the Odyssey, bands were quantified as follows: the integrated density of the bands was background subtracted and normalized to tubulin, GAPDH, or HSP90 prior to comparing protein levels between experimental and control lanes. Antibodies to BAF did not work with the Odyssey fluorescence scanner and were thus imaged using film. These blots were not quantified but were replicated 3 times to ensure the consistency of the phenotype.

Primary antibodies (human proteins)
Mouse anti–BAF (1:250; clone A11; sc-166324; Santa Cruz Biotechnology)
Rabbit anti–Lamin A/C (1:10,000; clone EPR4100; ab108595; Abcam)
Mouse anti–Lamin B1 (1:1,000; clone C12; sc-365214; Santa Cruz Biotechnology)
Mouse anti–Emerin (1:500; clone 4G5; EMERIN-CE; Leica Biosystems)
Rabbit anti–LEMD2 (1:1,000; HPA017340; Sigma-Aldrich)
Mouse anti–GAPDH (1:1,000; clone GT239; GTX627408; GeneTex)
Mouse anti–α-Tubulin (1:5,000; clone DM1A, GTX27291; GTX; GeneTex)
Rabbit anti-HSP90 (1:5000; 4874; Cell Signalling Technology)

Secondary antibodies
HRP-conjugated goat anti–mouse (1:5,000; G-21040; Thermo Fisher Scientific)
HRP-conjugated goat anti–rabbit (1:5,000; G-21234; Thermo Fisher Scientific)
HRP-conjugated goat anti–rabbit (1:5,000; G-21234; Thermo Fisher Scientific)
Alexa Fluor 790-conjugated donkey anti–rabbit (1:10,000; A-11374; Thermo Fisher Scientific)
Alexa Fluor 790-conjugated donkey anti–mouse (1:10,000; A-11371; Thermo Fisher Scientific)
Alexa Fluor 680-conjugated donkey anti–rabbit (1:10,000; A-10043; Thermo Fisher Scientific)
Alexa Fluor 680-conjugated donkey anti–mouse (1:10,000; A-10038; Thermo Fisher Scientific)

Immunofluorescence
Cells were grown on poly-L lysine coated coverslips and fixed with freshly made 3% paraformaldehyde (from 16% paraformaldehyde (w/v), EM grade; Electron Microscopy Sciences) in 1x PBS for 10 min at RT. Fixed cells were permeabilized with 1x PBS containing 0.4% Triton X-100 for 15 min, incubated with primary antibody for 1 hr, washed 3x5 min in 1x PBS, and incubated with secondary antibody for 1 hr. After the final antibody incubation, samples were washed for 3x5 min in 1x PBS, incubated in 0.1 ug/mL DAPI (Life Technologies) for 5 min, washed, and mounted in Vectashield (Vector Laboratories).

Primary antibodies
Rabbit anti–Lamin A/C (1:1,000; clone EPR4100; ab108595; Abcam)
Mouse anti–Lamin B1 (1:100; clone C12; sc-365214; Santa Cruz Biotechnology)
Mouse anti–Emerin (1:100; clone 4G5; EMERIN-CE; Leica Biosystems)
Rabbit anti–LEMD2 (1:100; HPA017340; Sigma-Aldrich)
Rabbit anti–cGAS (1:100; clone D1D3G; 15102S; Cell Signaling Technology)

Secondary antibodies
Alexa Fluor 488-conjugated goat anti–mouse (1:1,000; A-11029; Thermo Fisher Scientific)
Alexa Fluor 488-conjugated goat anti–rabbit (1:1,000; A-11034; Thermo Fisher Scientific)
Alexa Fluor 647-conjugated goat anti–mouse (1:1,000; A-21236; Thermo Fisher Scientific)
Alexa Fluor 647-conjugated donkey anti–rabbit (1:1,000; A-31573; Thermo Fisher Scientific)

Live cell imaging for NE rupture duration and GFP-BAF accumulation kinetics

Cells were grown in 8-well glass bottom µ-slides (ibidi) for imaging. For BAF, lamin A/C and emerin siRNA transfection, $1x10^4$ cells per well were seeded the day before transfection and transfected as described above with 100 nM siRNA final concentration. For LEMD2 knockdown the transfection reaction was added to the cells during seeding and again 24 hr post seeding. 4-6 hr after the last transfection, cells were incubated with 2 mM hydroxyurea (EMD Millipore). Cells were imaged starting 24 hr after hydroxyurea addition and imaged every 3 min for 24 hr or every 30 sec for 4 hr.

Live cell imaging for micronuclei
Cells were grown in 8-well glass bottom µ-slides (ibidi) and 0.5 µm reversine was added 4 hr prior to imaging. Cells were imaged every 3 min for 36 hr in the continued presence of 0.5 µm reversine.

Confocal microscopy
Live cell imaging was performed using a 20×/0.70 Plan Apo Leica objective on an automated Leica DMi8 microscope outfitted with an Andor CSU spinning disk unit equipped with Borealis illumination, an ASI automated stage with Piezo Z-axis top plate, and an Okolab controlled environment chamber (humidified at 37°C with 10% CO_2). Long term automated imaging was driven by MetaMorph software (version 7.10.0.119). Images were captured with an Andor iXon Ultra 888 EMCCD camera. All immunofluorescence imaging of fixed samples was performed using a 40x/1.30 Plan Apo Leica objective on a Leica DMi8 outfitted with a TCS SPE scan head with spectral detection. Images were acquired using the LAS X software platform (version 3.5.5.19976).

Image analysis
Fixed and live-cell images were adjusted for brightness and contrast and cropped and using ImageJ (Magalhaes *et al.*, 2004) or Photoshop 2019 (Adobe). Images and videos of cells expressing RFP-NLS were adjusted in the red channel by altering the gamma function to increase the visibility of cytoplasmic RFP. Images are single sections unless where noted.

For the fluorescence intensity trace analysis, images of nuclei expressing RFP-NLS and GFP-BAF were first background subtracted using a rolling ball (r = 150 px, sliding parabola), cropped to nucleus of interest, converted to 8-bit, and objects were identified by auto local intensity threshold algorithm (RFP-NLS), optimized to include only nuclear pixels during rupture events, or a single threshold set to exclude nucleus signals (GFP-BAF). Objects were analyzed for mean intensity (RFP-NLS) or integrated density (GFP-BAF) over time. To correct for focal drift, RFP-NLS values were normalized to the mean intensity of all nuclei in the field. Traces were visualized in Prism8 (GraphPad).

For analysis of nucleus integrity loss duration, time-lapse images of RFP-NLS expressing cells were evaluated by hand. Nucleus integrity loss duration were defined as the first frame that RFP-NLS was visible in the cytoplasm through every subsequent frame up to and including the first frame that RFP-NLS was no longer visible in the cytoplasm. Only cells that fit the following criteria were included in this duration analysis: (1) non-lobulated or multi-nucleated nucleus, (2) at least one rupture event occurs, (3) all rupture events are fully repaired, (4) cell is present in frame for at least 75% of imaging, and (5) cells did not undergo apoptosis. Cells were selected at random from multiple fields of view for each experiment. To eliminate bias, either a subset (>25%) or the entire dataset was blinded prior to analysis.

Statistical analysis
All statistical tests were all performed using Prism. Because our data did not have a normal distribution, nucleus integrity duration distributions were compared for significant differences in means or distributions using the Kolmogorov-Smirnov test (violin plot) and correlations were evaluated using Spearman's r statistic. Fisher's exact test was used to evaluate nominal data in the nucleus integrity loss duration histograms and NE rupture frequency on the raw numbers. Statistical analysis on histograms was done by first dividing each population into two groups: the duration under evaluation and all other values (e.g. 3 min versus not 3 min). These values were then tested against the values from other experimental conditions used Fisher's exact test with the null hypothesis that all samples had the same proportions of nucleus integrity durations. P-values were calculated for each replicate and if the p-values were homogenous between replicates, then the raw data was pooled and a final p-value calculated. If p-values were non-homogenous, then the comparison was reported as not "reproducible". Significance was determined if $P < 0.05$.

Acknowledgements

We would like to thank Dan Gerlich's lab at the Institute of Molecular Biotechnology of the Austrian Academy of Sciences for the BAF constructs. E.M.H is supported by the National Institutes of Health grant R35GM124766-02 and this project was funded in part through the NIH/NCI Cancer Center Support Grant P30CA015704. A.M. Y. is supported by the National Institutes of Health postdoctoral fellowship F32CA232764-01.

References

Anderson, D. J., and Hetzer, M. W. (2008). Reshaping of the endoplasmic reticulum limits the rate for nuclear envelope formation. J. Cell Biol. *182*, 911–924.

Appen, von, A., LaJoie, D., Johnson, I. E., Trnka, M., Pick, S. M., Burlingame, A. L., Ullman, K. S., and Frost, A. (2019). A role for liquid-liquid phase separation in ESCRT-mediated nuclear envelope reformation. bioRxiv *39*, 577460.

Barton, L. J., Soshnev, A. A., and Geyer, P. K. (2015). Networking in the nucleus: a spotlight on LEM-domain proteins. Curr Opin Cell Biol *34*, 1–8.

De Vos, W. H. *et al.* (2011). Repetitive Disruptions of the Nuclear Envelope Invoke Temporary Loss of Cellular Compartmentalization in Laminopathies

. Hum Mol Genet *20*, 4175–4186.

Denais, C. M., Gilbert, R. M., Isermann, P., McGregor, A. L., Lindert, Te, M., Weigelin, B., Davidson, P. M., Friedl, P., Wolf, K., and Lammerding, J. (2016). Nuclear envelope rupture and repair during cancer cell migration. Science *352*, aad7297–aad7358.

Deviri, D., Pfeifer, C. R., Dooling, L. J., Ivanovska, I. L., Discher, D. E., and Safran, S. A. (2019). Scaling laws indicate distinct nucleation mechanisms of holes in the nuclear lamina. Nature Physics 2019 *50*, 1.

Earle, A. J., Kirby, T. J., Fedorchak, G. R., Isermann, P., Patel, J., Iruvanti, S., Moore, S. A., Bonne, G., Wallrath, L. L., and Lammerding, J. (2019). Mutant lamins cause nuclear envelope rupture and DNA damage in skeletal muscle cells. Nat Mater *28*, 34.

Gatta, A. T., and Carlton, J. G. (2019). The ESCRT-machinery: closing holes and expanding roles. Curr Opin Cell Biol *59*, 121–132.

Gu, M. *et al.* (2017). LEM2 recruits CHMP7 for ESCRT-mediated nuclear envelope closure in fission yeast and human cells. Proc Natl Acad Sci U S A *114*, 201613916–E2175.

Halfmann, C. T., Sears, R. M., Katiyar, A., Busselman, B. W., Aman, L. K., Zhang, Q., O'Bryan, C. S., Angelini, T. E., Lele, T. P., and Roux, K. J. (2019). Repair of nuclear ruptures requires barrier-to-autointegration factor. J. Cell Biol. *114*, jcb.201901116.

Harada, T., Swift, J., Irianto, J., Shin, J.-W., Spinler, K. R., Athirasala, A., Diegmiller, R., Dingal, P. C. D. P., Ivanovska, I. L., and Discher, D. E. (2014). Nuclear lamin stiffness is a barrier to 3D migration, but softness can limit survival. J. Cell Biol. *204*, 669–682.

Haraguchi, T., Kojidani, T., Koujin, T., Shimi, T., Osakada, H., Mori, C., Yamamoto, A., and Hiraoka, Y. (2008). Live cell imaging and electron microscopy reveal dynamic processes of BAF-directed nuclear envelope assembly. J. Cell. Sci. *121*, 2540–2554.

Haraguchi, T., Koujin, T., Segura-Totten, M., Lee, K. K., Matsuoka, Y., Yoneda, Y., Wilson, K. L., and Hiraoka, Y. (2001). BAF is required for emerin assembly into the reforming nuclear envelope. J. Cell. Sci. *114*, 4575–4585.

Hatch, E. M., and Hetzer, M. W. (2016). Nuclear envelope rupture is induced by actin-based nucleus confinement. J. Cell Biol. *114*, jcb.201603053–36.

Hatch, E. M., Fischer, A. H., Deerinck, T. J., and Hetzer, M. W. (2013). Catastrophic nuclear envelope collapse in cancer cell micronuclei. Cell *154*, 47–60.

Houben, F. *et al.* (2013). Cytoplasmic localization of PML particles in laminopathies. Histochem Cell Biol *139*, 119–134.

Houthaeve, G., Robijns, J., Braeckmans, K., and De Vos, W. H. (2018). Bypassing Border Control: Nuclear Envelope Rupture in Disease. Physiology (Bethesda) *33*, 39–49.

Irianto, J. *et al.* (2017). DNA Damage Follows Repair Factor Depletion and Portends Genome Variation in Cancer Cells after Pore Migration. Curr Biol *27*, 210–223.

Isermann, P., and Lammerding, J. (2017). Consequences of a tight squeeze: Nuclear envelope rupture and repair. Nucleus *8*, 268–274.

Jamin, A., and Wiebe, M. S. (2015). Barrier to Autointegration Factor (BANF1): interwoven roles in nuclear structure, genome integrity, innate immunity, stress responses and progeria. Curr Opin Cell Biol *34*, 61–68.

LaJoie, D., and Ullman, K. S. (2017). Coordinated events of nuclear assembly. Curr Opin Cell Biol *46*, 39–45.

Liu, S., Kwon, M., Mannino, M., Yang, N., Renda, F., Khodjakov, A., and Pellman, D. (2018). Nuclear envelope assembly defects link mitotic errors to chromothripsis. Nature *561*, 551–555.

Maciejowski, J., Li, Y., Bosco, N., Campbell, P. J., and de Lange, T. (2015). Chromothripsis and Kataegis Induced by Telomere Crisis. Cell *163*, 1641–1654.

Magalhaes, P. J., Abramoff, M. D., and Ram, S. J. (2004). Image Processing with ImageJ. Biophotonics International *11*, 36–42.

Margalit, A., Segura-Totten, M., Gruenbaum, Y., and Wilson, K. L. (2005). Barrier-to-autointegration factor is required to segregate and enclose chromosomes within the nuclear envelope and assemble the nuclear lamina. Proc Natl Acad Sci U S A *102*, 3290–3295.

Olmos, Y., Hodgson, L., Mantell, J., Verkade, P., and Carlton, J. G. (2015). ESCRT-III controls nuclear envelope reformation. Nature *522*, 236–239.

Olmos, Y., Perdrix-Rosell, A., and Carlton, J. G. (2016). Membrane Binding by CHMP7 Coordinates ESCRT-III-Dependent Nuclear Envelope Reformation. Curr Biol *26*, 2635–2641.

Penfield, L., Shankar, R., Szentgyörgyi, E., Laffitte, A., Mauro, M., Audhya, A., Müller-Reichert, T., and Bahmanyar, S. (2019). Local regulation of lipid synthesis controls ER sheet insertion into nuclear envelope holes to complete nuclear closure. bioRxiv, 757013.

Penfield, L., Wysolmerski, B., Mauro, M., Farhadifar, R., Martinez, M. A., Biggs, R., Wu, H.-Y., Broberg, C., Needleman, D., and Bahmanyar, S. (2018). Dynein-pulling forces counteract lamin-mediated nuclear stability during nuclear envelope repair. Mol Biol Cell *29*, mbc.E17–06–0374–868.

Pfeifer, C. R. *et al.* (2018). Constricted migration increases DNA damage and independently represses cell cycle. Mol Biol Cell *29*, 1948–1962.

Raab, M. *et al.* (2016). ESCRT III repairs nuclear envelope ruptures during cell migration to limit DNA damage and cell death. Science *352*, aad7611–362.

Robijns, J., Molenberghs, F., Sieprath, T., Corne, T. D. J., Verschuuren, M., and De Vos, W. H. (2016). In silico synchronization reveals regulators of nuclear ruptures in lamin A/C deficient model cells. Scientific Reports *6*, 30325.

Salpingidou, G., Smertenko, A., Hausmanowa-Petrusewicz, I., Hussey, P. J., and Hutchison, C. J. (2007). A novel role for the nuclear membrane protein emerin in association of the centrosome to the outer nuclear membrane. J. Cell Biol. *178*, 897–904.

Samwer, M., Schneider, M. W. G., Hoefler, R., Schmalhorst, P. S., Jude, J. G., Zuber, J., and Gerlich, D. (2017). DNA Cross-Bridging Shapes a Single Nucleus from a Set of Mitotic Chromosomes. Cell *170*, 956–972.e23.

Santaguida, S., Tighe, A., D'Alise, A. M., Taylor, S. S., and Musacchio, A. (2010). Dissecting the role of MPS1 in chromosome biorientation and the spindle checkpoint through the small molecule inhibitor reversine. J. Cell Biol. *190*, 73–87.

Stephens, A. D. *et al.* (2019). Physicochemical mechanotransduction alters nuclear shape and mechanics via heterochromatin formation. Mol Biol Cell, mbcE19050286T.

Takaki, T. *et al.* (2017). Actomyosin drives cancer cell nuclear dysmorphia and threatens genome stability. Nat Commun *8*, 16013.

Tamiello, C., Kamps, M. A. F., van den Wijngaard, A., Verstraeten, V. L. R. M., Baaijens, F. P. T., Broers, J. L. V., and Bouten, C. C. V. (2013). Soft substrates normalize nuclear morphology and prevent nuclear rupture in fibroblasts from a laminopathy patient with compound heterozygous LMNA mutations. Nucleus *4*, 61–73.

Thaller, D. J., Allegretti, M., Borah, S., Ronchi, P., Beck, M., and Lusk, C. P. (2019). An ESCRT-LEM protein surveillance system is poised to directly monitor the nuclear envelope and nuclear transport system. eLife Sciences *8*, 33.

Vargas, J. D., Hatch, E. M., Anderson, D. J., and Hetzer, M. W. (2012). Transient nuclear envelope rupturing during interphase in human cancer cells. Nucleus *3*, 88–100.

Vietri, M. *et al.* (2019). Unrestrained ESCRT-III drives chromosome fragmentation and micronuclear catastrophe.

Vietri, M., Schink, K. O., Campsteijn, C., Wegner, C. S., Schultz, S. W., Christ, L., Thoresen, S. B., Brech, A., Raiborg, C., and Stenmark, H. (2015). Spastin and ESCRT-III coordinate mitotic spindle disassembly and nuclear envelope sealing. Nature *522*, 231–235.

Webster, B. M., Colombi, P., Jäger, J., and Lusk, C. P. (2014). Surveillance of nuclear pore complex assembly by ESCRT-III/Vps4. Cell *159*, 388–401.

Zhang, Q., Tamashunas, A. C., Agrawal, A., Torbati, M., Katiyar, A., Dickinson, R. B., Lammerding, J., and Lele, T. P. (2019). Local, transient tensile stress on the nuclear membrane causes membrane rupture. Mol Biol Cell *30*, 899–906.

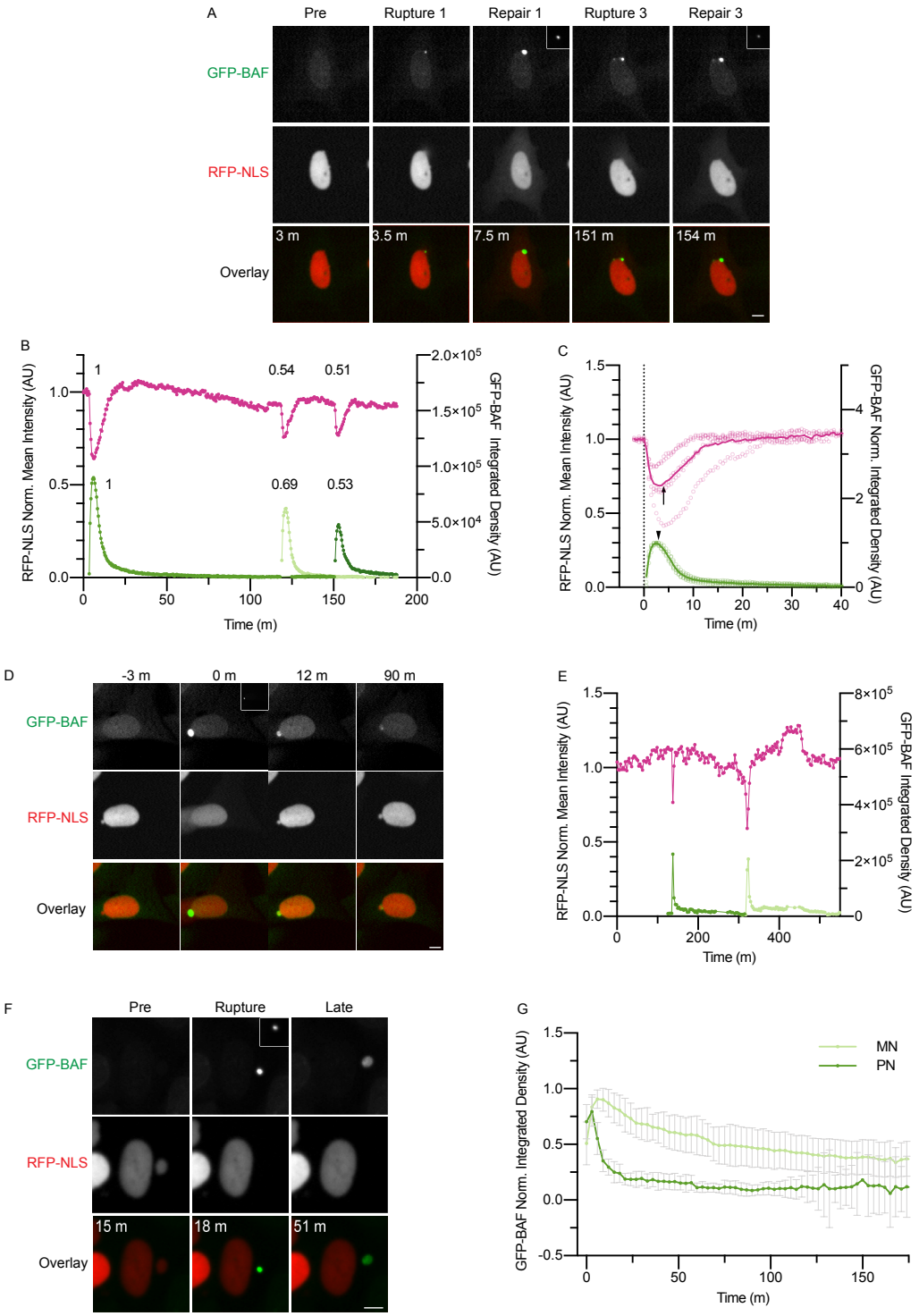

Figure 1. Characterization of GFP-BAF accumulation and loss kinetics at membrane rupture sites. (A) Still images of U2OS GFP-BAF, 2xRFP-NLS (RFP-NLS), shRNA-LmnB1 cells imaged every 30 sec for 4 hr. RFP-NLS images gamma adjusted for visibility of cytoplasmic RFP, insets are unsaturated images of GFP-BAF at rupture sites. m = minutes post imaging start. (B) Traces of nuclear RFP-NLS mean intensity (RFP-NLS_{Nuc}, red) and GFP-BAF integrated density (GFP-BAF_{ID}, green) of 3/4 rupture sites in cell (A). Decreases in RFP-NLS_{Nuc} coincide with the appearance of RFP-NLS in the cytoplasm, indicating ruptures. Values above the RFP trace indicate the extent of RFP-NLS_{Nuc} decrease during rupture, relative to the first rupture. Values on the GFP trace indicate the maximum GFP-BAF intensity relative to the first rupture. (C) Traces of RFP-NLS_{Nuc} and GFP-BAF_{ID}, normalized to maximum intensity, for ruptures lasting 5 min or less. Mean (thick line) and replicate values (open circles) are plotted. Arrow = first increase in RFP-NLS_{Nuc} intensity after rupture, arrowhead = first decrease in GFP-BAF_{ID}. n = 5 ruptures. (D) Still images of U2OS GFP-BAF RFP-NLS shLmnB1 cells imaged every 3 min. BAF accumulation at the membrane rupture site is visible 78 min after RFP-NLS_{Nuc} reaccumulates. (E) Traces of RFP-NLS_{Nuc} and GFP-BAF_{ID} for each of 2 ruptures visible in cell (D). GFP-BAF_{ID} was recorded until an object was no longer distinguishable or another rupture occurred. (F) Still images of U2OS GFP-BAF RFP-NLS shLmnB1 cells undergoing micronucleus rupture (imaged every 3 min). (G) Normalized average intensity traces of GFP-BAF_{ID} from micronuclei (MN) or primary nuclei (PN) ruptures. Average intensity and 95% CI are plotted for n = 8 MN ruptures and 13 PN ruptures. Scale bars = 10 µm. AU = arbitrary units.

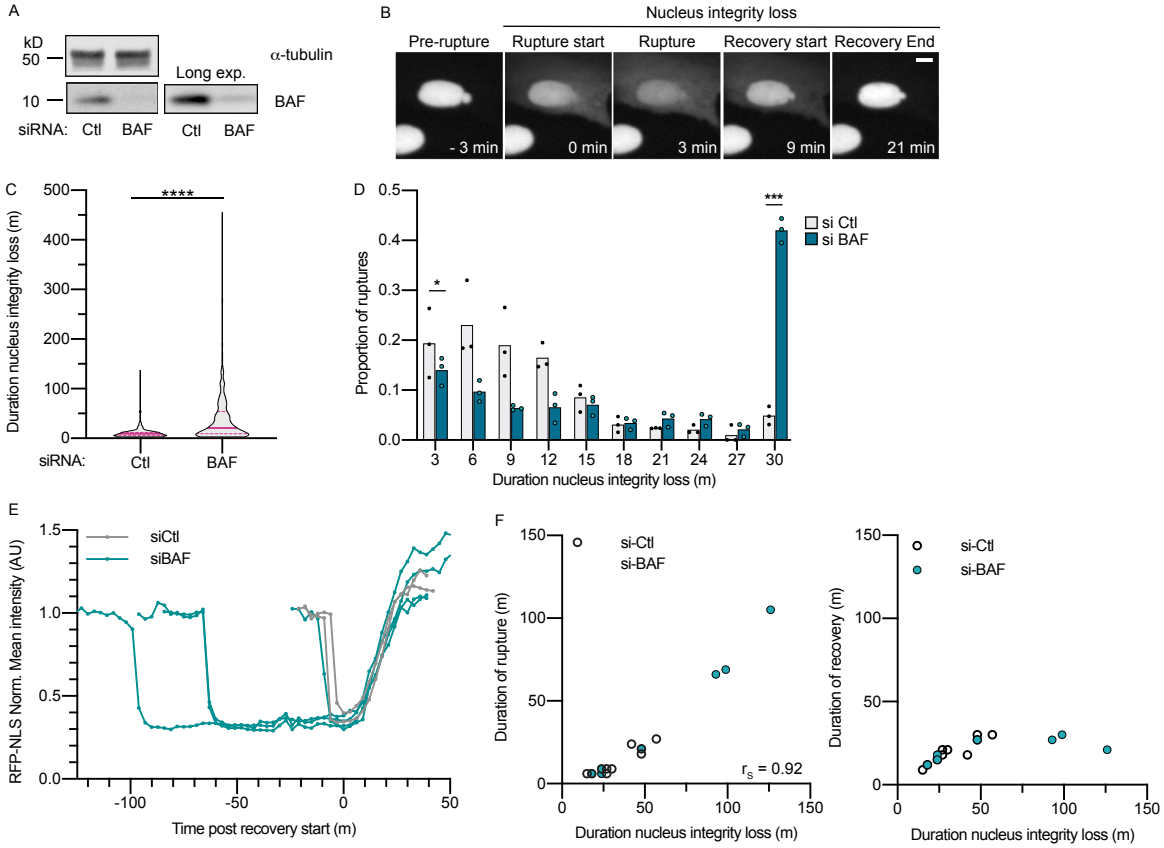

Figure 2. BAF depletion delays nuclear membrane repair. (A) Representative immunoblot of BAF protein levels 48 hr after siRNA transfection. A longer exposure is shown at right. (B) Still images of U2OS RFP-NLS shLmnB1 cells. Duration of nucleus integrity loss quantified as the number of frames with cytoplasmic RFP-NLS+1, multiplied by 3 min. Scale bar = 10 µm. (C) Violin plot of nucleus integrity loss duration for individual rupture events occurring in cells treated with the indicated siRNAs. $n_{siControl}$ = 416 and n_{siBAF} = 387, over 3 experiments. ****p<0.0001, Kolmogorov-Smirnov (K-S) test. (D) Histogram of proportion of ruptures shown in (C) with indicated durations of nucleus integrity loss. Graph depicts mean (bar) and replicates (dots) from 3 experiments. ***p<0.001, *p<0.05, Fisher's exact test. (E) Trace analysis of RFP-NLS_{Nuc} from ruptures where nucleus integrity loss lasts 30 min or more from siControl and siBAF cells. t_0 = the first consistent increase in RFP-NLS_{Nuc}, which marks the division between rupture and recovery (indicated on graph). $n_{siControl}$ = 3; n_{siBAF} = 4. (F) Duration of rupture (left) and duration of recovery (right), determined from traces of RFP-$NLS_{Nuc.,}$ compared to duration of nucleus integrity loss for individual ruptures from siControl and siBAF cells. $n_{siControl}$ = 10; n_{siBAF} = 9. r_S = Spearman r correlation for combined ruptures.

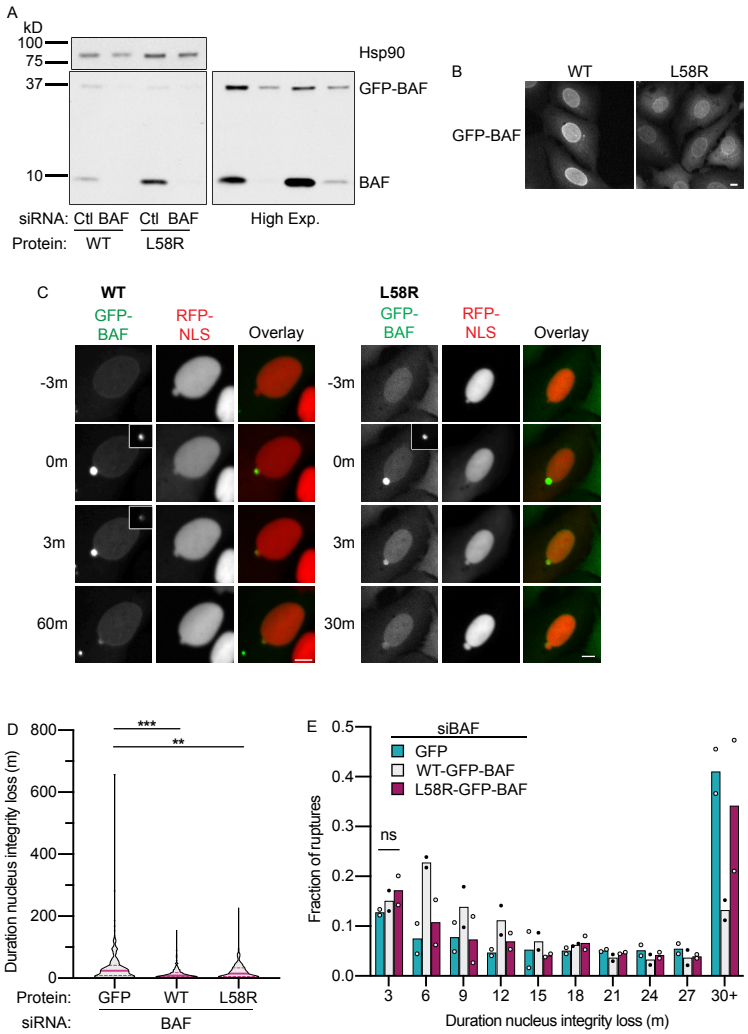

Figure 3. BAF LEM-protein binding function is required for efficient nuclear membrane repair. (A) Representative immunoblot of BAF protein levels in U2OS RFP-NLS shLmnB1 expressing either WT-GFP-BAF or L58R-GFP-BAF for 48 hr after depletion of endogenous BAF. A longer exposure is shown at right. (B) Representative images of non-transfected cells expressing either WT- or L58R-GFP-BAF. (C) Still images of U2OS RFP-NLS shLmnB1 cells expressing either WT- or L58R-GFP-BAF and transfected with siBAF. T_0 = rupture start (Figure 2B). (D) Violin plot of nucleus integrity loss duration for individual rupture events occurring in cells expressing indicated proteins and treated as in (C). $n_{siBAF, GFP}$ = 235, $n_{siBAF, WT\text{-}GFP\text{-}BAF}$ = 228, $n_{siBAF, L58R\text{-}GFP\text{-}BAF}$ = 321, from 2 experiments. ***p<0.001, **p<.01 K-S test. (E) Histogram of proportion of ruptures shown in (D) with indicated duration of nucleus integrity loss.

Graph depicts mean (bar) and replicates (dots) from 2 experiments. P = ns, Fisher's exact test. Scale bars = 10 µm.

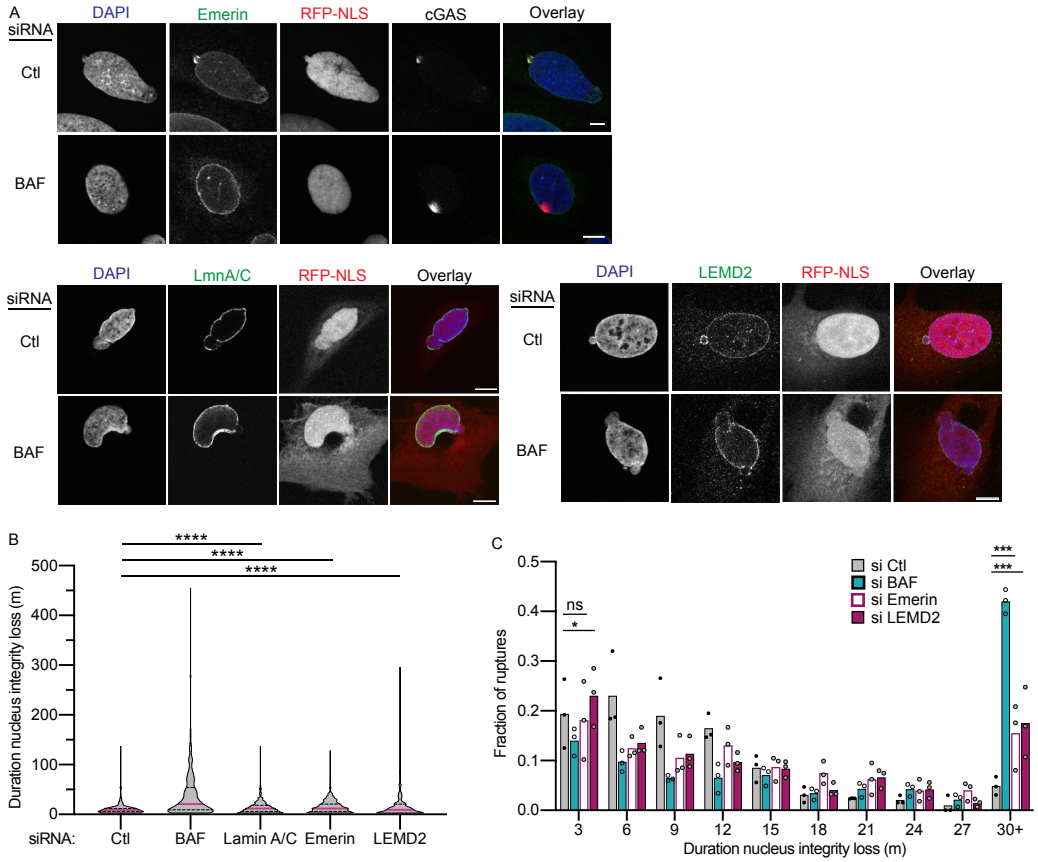

Figure 4. BAF recruits emerin and LEMD2 to accelerate nucleus recompartmentalization. (A) Representative images of U2OS RFP-NLS shLmnB1 cells transfected with siControl or siBAF undergoing nuclear membrane rupture, determined by cGAS accumulation or cytoplasmic RFP-NLS. Cells were labeled with antibodies to emerin, lamin A/C, or LEMD2. Scale bars = 10 µm. (B) Violin plot showing the distribution of nucleus integrity loss duration for individual rupture events in cells transfected with siRNAs against either emerin, lamin A/C, LEMD2 48 hr prior to imaging. Data for siControl and siBAF are reproduced from Figure 2C for comparison. $n_{siEmerin} = 416$; $n_{siLmnA/C} = 548$; $n_{LEMD2} = n = 887$, from 3 experiments. ****p<0.0001, K-S test. (C) Histogram of proportion of ruptures shown in (B) with indicated duration of nucleus integrity loss. Graph depicts mean (bar) and replicates (dots) from 3 experiments. ***p<0.001, *p<0.05, p = ns, Fisher's exact test.